ARTICLE

Direction observation of the grain boundary segregation in molybdenum substituted lanthanum tungstate membranes

Received 00th January 20xx,
Accepted 00th January 20xx

DOI: 10.1039/x0xx00000x

Ke Ran,*[a,b] Wendelin Deibert,[c] Mariya E. Ivanova,[c] Wilhelm A. Meulenberg,[c,d] and Joachim Mayer[a,b]

Molybdenum substituted lanthanum tungstate membranes (LWO-Mo) offer a good alternative for the separation of hydrogen from gas mixtures. During several essential steps of the membrane processing, an intensive employment of ZrO_2 milling balls is usually inevitable. However, how these milling balls affect the final LWO-Mo membranes, is still largely unknown. Employing comprehensive transmission electron microscopy (TEM) techniques, the residual Zr was found to segregate to the grain boundaries (GBs) of the LWO-Mo, either as thin layers or as individual nanograins. At atomic scale, structural and chemical analyses on these GB features were carried out quantitatively. The segregated Zr took more than half of the W sites of the LWO-Mo, resulting in a strained LWO structure and locally concentrated oxygen vacancies. To minimize any Zr contamination, either a competent alternative for ZrO_2 or a careful introduction of certain secondary phases (SPs) was proposed. Our results unravel the processing-induced GB behaviors in LWO-Mo, which pave the way towards further optimized processing for various types of functional membranes.

1. Introduction

As a mixed protonic and electronic conductor, lanthanum tungstate (LWO)[1-3] has received increasing research interests for its application in hydrogen separation.[4-8] To overcome the lack of electronic conductivity of pure LWO below 700 °C,[1] various strategies have been proposed, including dual phase composite membranes,[9-11] fluoride-anion doping in the LWO membranes,[12] and substitution of W by the more reducible Mo or Re.[5, 7, 13-15] Moreover, asymmetric membrane structures were designed, in which the thickness of the gas separation layer is significantly reduced, and different porous substrates such as LWO and MgO were employed as mechanical support.[16-18]

In addition to the bulk conductivity of individual LWO grains, grain boundaries (GBs) play an important role as well in the separation performance of the membranes. Theoretically, the GBs can be either positive for the total conductivity[19] or be the blocking factor for the membrane permeation.[20] In order to systematically control the GB microstructure and finally to achieve a better separation performance, precise information about the structure and chemistry at the grain boundaries is indispensable. However, compared with the intensive studies on tuning the bulk conductivity of the LWO grains, only few results have been reported thus far concerning the behaviors of the GBs inside the LWO membranes.

Transmission electron microscopy (TEM) with atomic resolution provides unique advantages in studying the GBs.[21] In mixed ionic-electronic conductors, the charge distribution and chemical environments along GBs were revealed using TEM imaging and spectroscopy approaches, and further linked with a superior GB ionic conductivity.[19] Utilizing electron energy loss spectroscopy (EELS), an increase in the concentration of the oxygen vacancies was observed in the GB cores of the fluorite-structured materials.[22] Amorphous intergranular phases were directly identified by high-angle annular dark-field (HAADF) imaging, which are responsible for substantial retardation of proton migration and instability of the proton-conducting $BaCeO_3$ polycrystals.[20]

In this work, a comprehensive TEM study is carried out, focusing on the GBs inside LWO membranes, in which nominally 20 mol.% of the W sites are occupied by Mo ($La_{5.4}W_{0.8}Mo_{0.2}O_{12-\delta}$, LWO-Mo). For the first time, the structural and chemical changes caused by the GB segregation are quantitatively identified down to atomic scale. Origin of the GB segregation, its potential effects on the performance of the LWO-Mo membranes, as well as possible solutions will be discussed in detail.

[a] Central Facility for Electron Microscopy GFE, RWTH Aachen University, 52074 Aachen, Germany.
E-mail: ran@gfe.rwth-aachen.de
[b] Ernst Ruska-Centre for Microscopy and Spectroscopy with Electrons ER-C, Forschungszentrum Jülich GmbH, 52425 Jülich, Germany.
[c] Institute of Energy and Climate Research IEK-1, Forschungszentrum Jülich GmbH, 52425 Jülich, Germany.
[d] Faculty of Science and Technology, Inorganic Membranes, University of Twente, 7500 AE Enschede, The Netherlands.
† Electronic Supplementary Information (ESI) available. See
DOI: 10.1039/x0xx00000x

2. Experimental methods

2.1 LWO-Mo membrane preparation

Ceramic powder of LWO-Mo (20 mol% W substituted by Mo) was synthesized by the solid state route at 1100 °C for 5 h in air. First, the stoichiometric amounts of $La(OH)_3$, WO_3 and MoO_3 were mixed in ethanol with ZrO_2 milling balls for 24 h on a rolling bench. The rotation speed was 30 min^{-1}. After this, the powder showed a particle size of D50 = 0.54 µm and a specific area A_{spec} = 2.7 m^2/g which appeared suitable for tape casting without any further treatment. The LWO-Mo membrane was prepared by tape casting which is a well-established manufacturing route for ceramic component of planar architecture.[8, 16] During the process, the self-produced ceramic powder was first transferred into a suspension, which additionally contained a solvent, binder, plasticizer and dispersing agent. All components were then mixed in a planetary mixer with a rotation speed of 1000 min^{-1} for 3 min and then of 1500 min^{-1} for 3 min assisted by the ZrO_2 milling balls to get a homogeneous suspension. Then, the suspension was applied on a moving polymeric foil using tape cast device KAROcast300-7 by KMS Automation GmbH Germany. The layer thickness was adjusted with a blade, which ensured a uniform gap of 250 µm for the suspension on the foil. After tape drying, samples were shaped off the tape and sintered at 1450 °C for 6 h in air. The final membrane consisted of one dense single layer with a thickness around 80 µm.

2.2 TEM sample preparation

Plan view scanning electron microscopy (SEM) sample was prepared from the as-synthesized LWO-Mo membrane by grinding and polishing. Focused ion beam (FIB) lamellas were cut from the plan view SEM sample using an FEI Helios NanoLab 400S system with a Ga ion beam.[23] Further thinning and cleaning were performed with an focused Ar ion beam in a Fischione Nanomill 1040 at 900 and 500 eV beam energy respectively.

2.3 Characterization techniques

Electron diffractions were performed by FEI Tecnai F20 at 200 kV. High resolution HAADF imaging, energy dispersive X-ray (EDX) chemical mapping and EELS spectrum imaging with atomic resolution were conducted with an FEI Titan G2 80-200 ChemiSTEM microscope equipped with an XFEG, a probe Cs corrector, a super-X EDXS system, and a Gatan Enfinium ER (model 977) spectrometer with DUAL EELS acquisition capability.[24] The convergence semi-angle for STEM imaging and EDX chemical mapping was approximately 22 mrad, while the collection semi-angles were 88-220 mrad for HAADF imaging and around 47 mrad for EELS spectrum imaging. EDX maps were collected typically for ~10 minutes, and background subtraction was performed. EELS spectrum images were recorded with 0.5 eV/channel energy dispersion and 0.1 s dwell time for each pixel. Multivariate statistical analysis (MSA) was performed to reduce the noise of the ELL spectra with weighted principle-component analysis (PCA). To improve the image quality, the HAADF images were first averaged from a series of frames with a relatively short exposure time by an iterative rigid alignment algorithm[25] and then smoothed by a nonlinear filtering algorithm.[26] Structural models were visualized with VESTA.[27] The SEM investigation was carried out by JEOL JSM7000F, and the XRD measurements were performed with a Bruker D4 X-ray diffractometer.

3. Results

Based on SEM imaging in Fig. 1a, the LWO-Mo membranes show compact grains, with various sizes ranging from several µm to tens of µm.[28, 29] The XRD result reveals that the LWO-Mo is predominantly composed of grains with the LWO fluorite structure (see Fig. S1 in the ESI†). The HAADF image in Fig. 1b shows a junction of three LWO-Mo grains, G1, G2 and G3. Among them, G3 is oriented along the [101] direction and thus appears brighter than G1 and G2, which are both randomly oriented. Along the GBs, relatively lower contrast with a

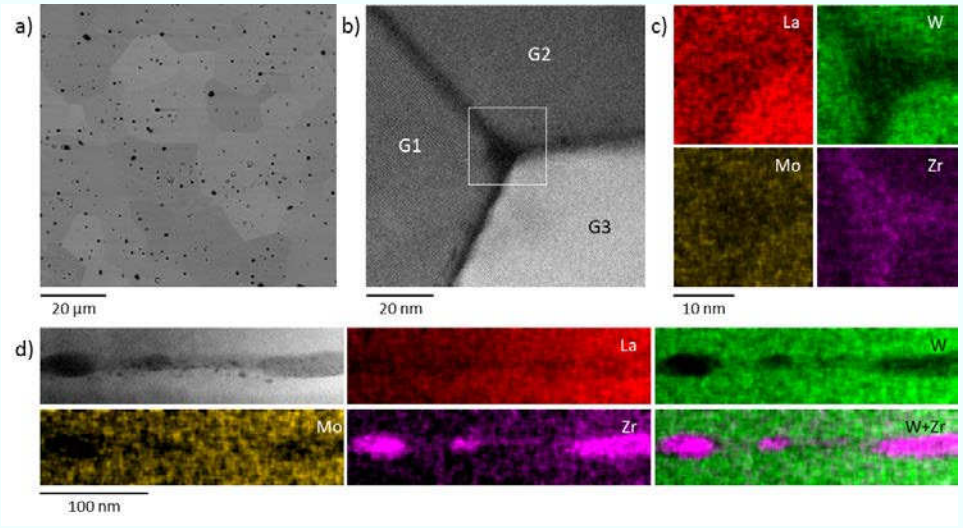

Fig. 1 An overview of the grain boundary segregations. (a) Plan view SEM image of the LWO-Mo membrane.[29] (b) HAADF image showing the junction of three LWO-Mo grains, G1-G3. G3 is oriented along the [101] direction, while G1 and G2 are randomly oriented. (c) EDX elemental maps of La *Lα*, W *Lα*, Mo *Lα*, and Zr *Lα* corresponding to the central squared region in (b). (d) HAADF image and EDX elemental maps around an interface between two LWO-Mo grains.

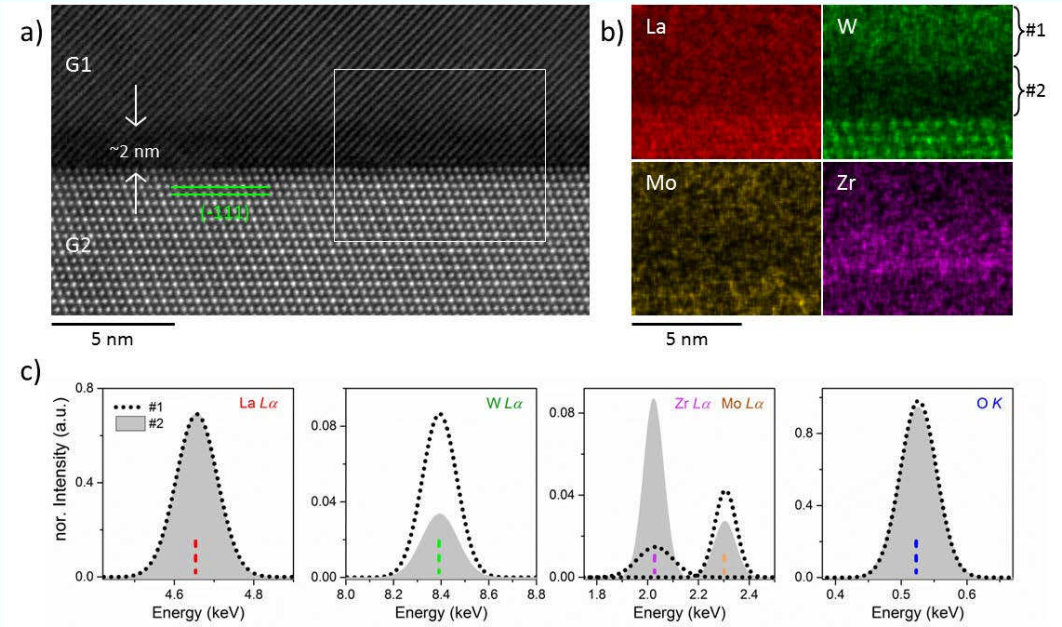

Fig. 2 Grain boundary segregation between LWO-Mo grains. (a) HAADF image of the interface between two LWO-Mo grains, G1 and G2. G1 is close to the [001] direction. G2 is oriented along the [101] direction and ending with the (-111) plane. (b) EDX elemental maps from the rectangle area in (a). Next to the W map, two regions are defined by the brackets as #1 and #2. (c) The La *Lα*, W *Lα*, Zr *Lα*, Mo *Lα* and O *K* peaks from region #1 and #2, after background subtraction, normalization and fitting with Gaussian function. Dashed lines indicate the energy of each peak.

at. %	La/W	La/O	W/(W+Mo+Zr)	Mo/(W+Mo+Zr)	Zr/(W+Mo+Zr)
#1	6.75	0.49	0.8	0.2	-
#2	16.59±1.14	0.48±0.01	0.33±0.02	0.13±0.01	0.54±0.03

Table 1 The estimated chemical composition for region #2 in Fig. 2b, by taking region #1 as an internal standard.

thickness of several nm can be noticed. The central squared region in Fig. 1b was then selected for EDX mapping, and the corresponding elemental maps of La, W, Mo and Zr are shown in Fig. 1c. Significant loss of W and considerable enrichment of Zr can be noticed simultaneously along all the GBs. Besides, G3 shows a higher intensity in the La, W and Mo maps, which is also due to its orientation along the [101] zone axis.

In contrast to Fig. 1b-c, the Zr segregations in Fig. 1d were observed as individual nanograins along the GB. These nanograins have various lengths parallel to the GB, but are mainly confined within ~20 nm in the direction vertical to the GB. They are shared by the two neighboring LWO-Mo grains without clear preference. A similar chemical behavior as observed in Fig. 1c, *i.e.* simultaneously loss of W and enrichment of Zr, is noticed inside these nanograins as well.

3.1 GB segregation between LWO-Mo grains

Fig. 2a shows a sharp interface between two LWO-Mo grains, G1 and G2. Here, G1 is close to the [001] direction, and therefore some lattice fringes are still visible (see Fig. S2 in the ESI†). G2 is oriented along the [101] direction and separated from G1 through the (-111) plane, as indicated by the solid lines. Relatively lower contrast with a thickness around 2 nm can be noticed along the interface and mainly on the G1 side.

The EDX elemental maps in Fig. 2b were collected from the rectangle area in Fig. 2a. For quantification, EDX signals from the two regions, #1 and #2 as marked by the brackets next to the W map, were extracted, respectively. After background subtraction and normalization, the La *Lα*, W *Lα*, Zr *Lα*, Mo *Lα* and O *K* peaks were fitted with Gaussian function and plotted in Fig. 2c. A comparison between the experimental and fitted spectra can be found in Fig. S2 in the ESI†. The La and O peaks from region #1 and #2 are quite similar, suggesting consistent contents of La and O in both regions. Comparing with region #1, region #2 gives obviously lower W and Mo peaks, but significantly higher Zr peak. For region #1, a small Zr peak is detected as well. It can be attributed to the possible delocalization of the EDX signals, and the contributions from the minor W *Mγ* peak at 2.038 keV and Mo *Ll* peak at 2.016 keV, which are both close to the Zr *Lα* peak at 2.042 keV.

Under the specific viewing condition in Fig. 2a, little overlap of G1 and G2 would be expected within region #1 or #2. Thus, region #1 can be considered as pure LWO-Mo with the nominal composition $La_{5.4}W_{0.8}Mo_{0.2}O_{11.1}$, and region #2 is the LWO-Mo modified by GB segregation. The intensities under the La, W, Mo and O peaks in Fig. 2c were then integrated. Taking region #1 as an internal standard, the *k* factors can be calibrated and used to estimate the atomic ratios of La/O, W/(W+Mo+Zr), Mo/(W+Mo+Zr) and Zr/(W+Mo+Zr) in region #2,

$$k_{A/B} = \frac{A_{at.\%,\#1}}{B_{at.\%,\#1}} \times \frac{B_{counts,\#1}}{A_{counts,\#1}}$$

$$\frac{\mathrm{A_{at.\%,\#2}}}{\mathrm{B_{at.\%,\#2}}} = \mathrm{k_{A/B}} \times \frac{\mathrm{A_{counts,\#2}}}{\mathrm{B_{counts,\#2}}}$$

, where $\mathrm{A_{at.\%,\#1}}$ is the composition of element A in atomic percent in region #1, and $\mathrm{A_{counts,\#1}}$ is the integrated counts under the selected peak of element A in region #1.

The error of AB/CD was obtained according to

$$\sigma_{\mathrm{AB/CD}} = \frac{\mathrm{AB}}{\mathrm{CD}} \sqrt{\left(\frac{\sigma_{\mathrm{A}}}{\mathrm{A}}\right)^2 + \left(\frac{\sigma_{\mathrm{B}}}{\mathrm{B}}\right)^2 + \left(\frac{\sigma_{\mathrm{C}}}{\mathrm{C}}\right)^2 + \left(\frac{\sigma_{\mathrm{D}}}{\mathrm{D}}\right)^2}.$$

The estimated atomic ratios in region #1 and #2 are listed in Table 1. Due to the significant W loss, the La/W ratio increases dramatically in region #2. Consistent with the comparable La and O peaks in Fig. 2c, the La/O ratio of 0.48 in region #2 is close to the nominal value of 0.49. Since the La contents in region #1 and #2 are nearly the same, and the fluorite structure of LWO is mainly preserved even with the GB segregation (as will be discussed later), all the Zr in region #2 can only take the W sites. Thus, assuming a La/(W+Mo+Zr) ratio of 5.4, the distribution of all the W sites among W, Mo and Zr is calculated. Inside region #2, more than half of the W sites (54%) are found to be occupied by Zr.

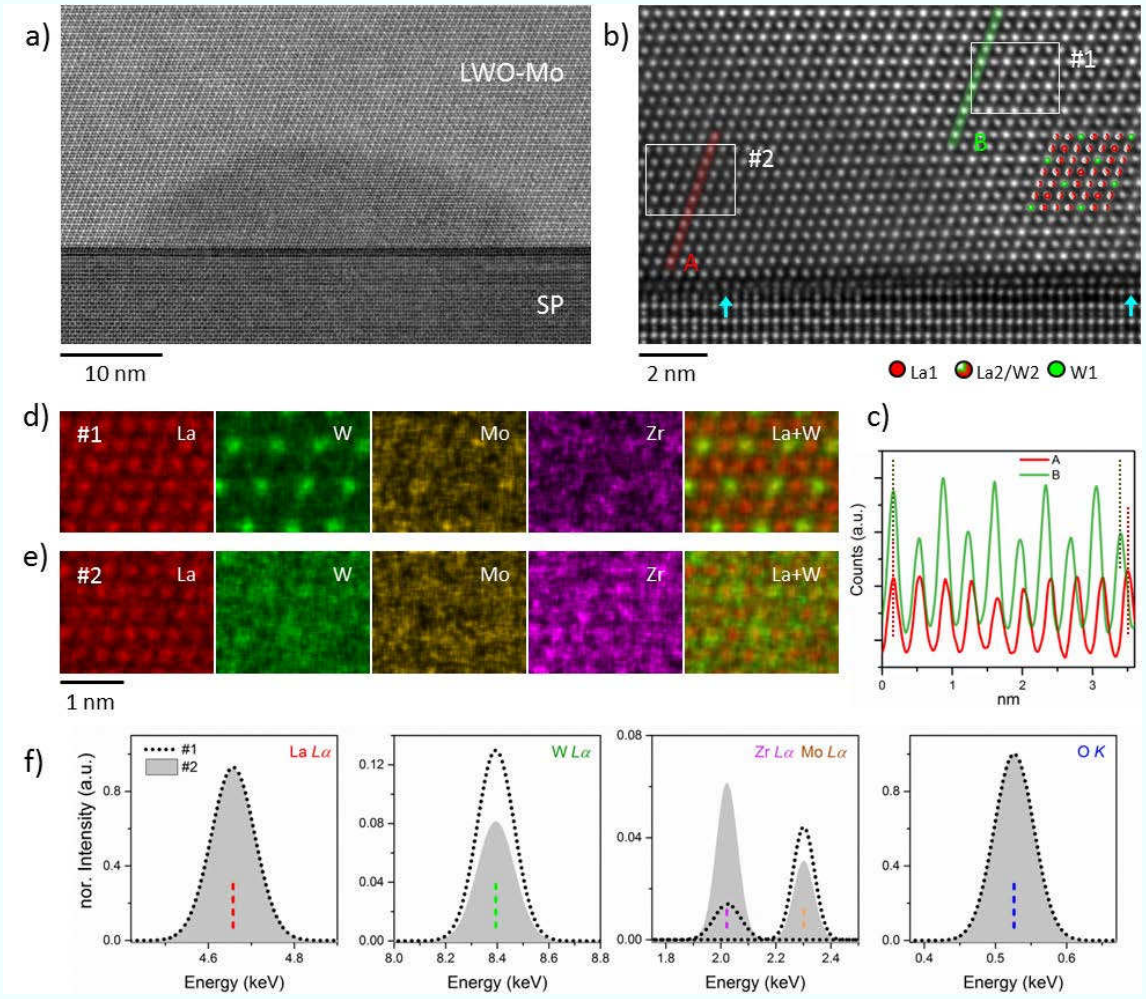

Fig. 3 Grain boundary (GB) segregation between the LWO-Mo and the secondary phase (SP). (a) HAADF image showing the GB segregation located as a nanograin between the LWO-Mo and SP (determined as $La_{2/3}(Mg_{1/2}W_{1/2})O_3$). The LWO-Mo is oriented along the [101] direction. (b) HAADF image of an interface between the LWO-Mo/nanograin and the SP. Inset on the right is the average LWO model oriented along [101] direction. A broken atomic layer of the SP is indicated by the pair of arrows. (c) Intensity profiles along the plane A and B as defined in (b). (d-e) EDX elemental maps recorded from the rectangles labeled as #1 and #2 in (b). (f) The La *La*, W *La*, Zr *La*, Mo *La* and O *K* peaks from region #1 and #2, after background subtraction, normalization and fitting with Gaussian function. Dashed lines indicate the energy of each peak.

at. %	La/W	La/O	W/(W+Mo+Zr)	Mo/(W+Mo+Zr)	Zr/(W+Mo+Zr)
#1	6.75	0.49	0.8	0.2	-
#2	10.78±0.25	0.49±0.01	0.50±0.01	0.13±0.02	0.37±0.03

Table 2 The estimated chemical composition for rectangle #2 in Fig. 3b, by taking region #1 as an internal standard.

3.2 GB segregation between the LWO-Mo and the secondary phase

As shown in Fig. 1d, between two LWO-Mo grains, the Zr segregations in the form of individual nanograins are normally located with poorly defined shapes (see Fig. S2 in the ESI†). Challenges to directly investigate these nanograins down to atomic scale include their limited sizes especially in the direction vertical to the interface, their different orientations comparing with the neighboring LWO-Mo grains, and the common overlap of three components (the nanograin and the two LWO-Mo grains) along the viewing direction. Meanwhile, for the investigated membranes, in addition to the primary LWO-Mo phase, a few secondary phase (SP) grains were occasionally located[29] (see Fig. S4 in the ESI†). Between the LWO-Mo and the SP, nanograins with better defined shapes can be found. These nanograins share similar structural and chemical features as those located between LWO-Mo grains, and thus enable an in-depth study on the GB segregation down to the atomic scale.

Such a nanograin is shown in Fig. 3a. It has a hillock shape, attached to the interface from the LWO-Mo side. The LWO-Mo is oriented along the [101] direction, while the nanograin shows a similar crystal structure but a lower contrast. The SP was identified as $La_{2/3}(Mg_{1/2}W_{1/2})O_3$ in another work,[29] and the dark interface is a result of the complete depletion of W in the contacting atomic planes from both sides.

Fig. 3b is the closer look of a nanograin located between the LWO-Mo and the SP ($La_{2/3}(Mg_{1/2}W_{1/2})O_3$). Intensity profiles along plane A and B, as defined by the red and green lines, are first compared in Fig. 3c. Without any modulation, plane A shows a much lower intensity than plane B. Moreover, as indicated by the dotted lines in Fig. 3c, a slightly larger lattice constant can be determined from plane A. Besides, in Fig. 3b, the first atomic plane of the SP is noticed to end abruptly when going from the right side (the LWO-Mo) to the left side (the nanograin), as marked by the pair of arrows.

The EDX elemental maps in Fig. 3d and 3e are collected from the rectangle #1 and #2 in Fig. 3b. All the maps in Fig. 3d show a good agreement with the LWO model, and several local maxima of Mo are detected at the W sites. In contrast, the La map in Fig. 3e still follows the LWO model, but any local maximum in the W or Mo map is barely detectable. The composite maps of La and W in Fig. 3d-e further illustrate the chemical difference between the LWO-Mo and the nanograin. Fig. 3f compares the major peaks extracted from both mappings, which show similar behaviors as in Fig. 2c. Taking the rectangle #1 as an internal standard, the chemical composition inside rectangle #2 was determined following the same method described above. As listed in Table 2, a La/O ratio of 0.49 is estimated for rectangle #2, almost the same as inside the LWO-Mo. Besides, around 37% of the W sites inside rectangle #2 are occupied by Zr.

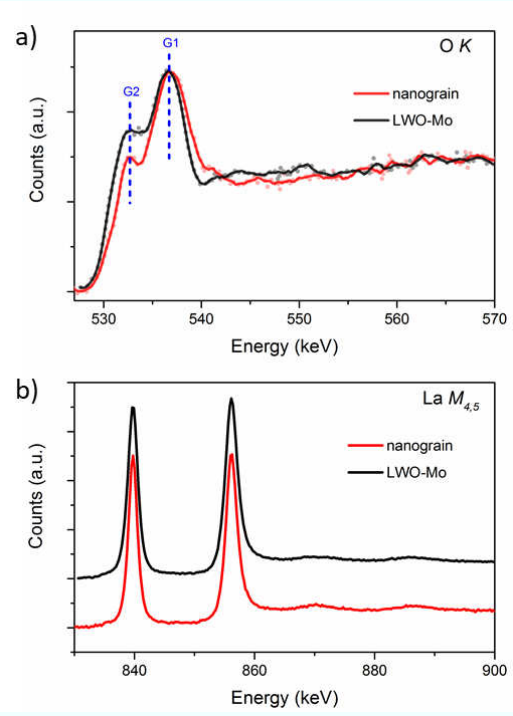

Fig. 4 EELS spectra showing the O *K* (a) and La $M_{4,5}$ (b) edge recorded from the nanograin and the LWO-Mo. The spectra in (b) are offset in the vertical direction.

3.3 Oxygen vacancies generated by the GB segregation

The ionic conductivity of the LWO-Mo membrane is highly sensitive to the behavior of the oxygen vacancies. Although the EDX quantifications in Table 1 and 2 suggest almost equal oxygen content for regions with and without Zr segregation, differences might be overlooked due to the absorption of the O *K* line, which lies in a relatively low energy range for the EDX. As a complementary technique, EELS is more sensitive to the light elements, and therefore is employed to study the fine structure of the O *K* edge.

The EELS spectra in Fig. 4 compare the O *K* and La $M_{4,5}$ edges from the nanograin and the LWO-Mo, which were collected from the same region as in Fig. 3b (see Fig. S6 in the ESI†). In Fig. 4b, consistent La $M_{4,5}$ edges are obtained. Both O *K* edges in Fig. 4a show a twin-peak feature, similar as those reported in cerium stabilized zirconia.[30] However, the smaller peak labeled as G2 from the nanograin is much lower than that from the LWO-Mo. Further analysis indicates that both the shape and position of G2 are closely related to the W1 site occupation (see Fig. S6 in the ESI†).

The intensities under the O *K* and La $M_{4,5}$ edges in Fig. 4 are then integrated. The La/O ratios are estimated as $\frac{La}{O}_{LWO-Mo} / \frac{La}{O}_{nanograin} \cong 0.967$. Since the content of La stays the same for both regions, the average oxygen vacancy within one unit cell will thus increase by ~1.83, *i.e.* from 0.5 for LWO-Mo ($La_{27}W_4Mo_1O_{55.5}v_{0.5}$) to 2.33 for the nanograin. In Table 2, the EDX measurement suggests that up to 37% of the W sites are occupied by Zr. Thus, within one unit cell, 1.85 out of the 5 W sites will be occupied by Zr^{4+} instead of W^{6+} or Mo^{6+}. Due to this acceptor dopant, Zr''_W, additional 1.85 oxygen vacancies will be created, which is in a good agreement of the value of 1.83 estimated from the EELS measurement.

3.4 Structural changes accompanying the GB segregation

The abrupt ending of atomic plane in Fig. 3b and the mismatched lattice constant in Fig. 3c indicate structural disorders caused by the GB segregation. The HAADF image in Fig. 5a shows another nanograin between the LWO-Mo and the SP. The SP here is identified as $La_6W_2O_{15}$ with W partially substituted by Mo and Zr (see Fig. S4-5 in the ESI†). The LWO-Mo in Fig. 5a is oriented along the [101] zone axis and separated from the nanograin through a series of (-111), (11-1) and (010) planes.

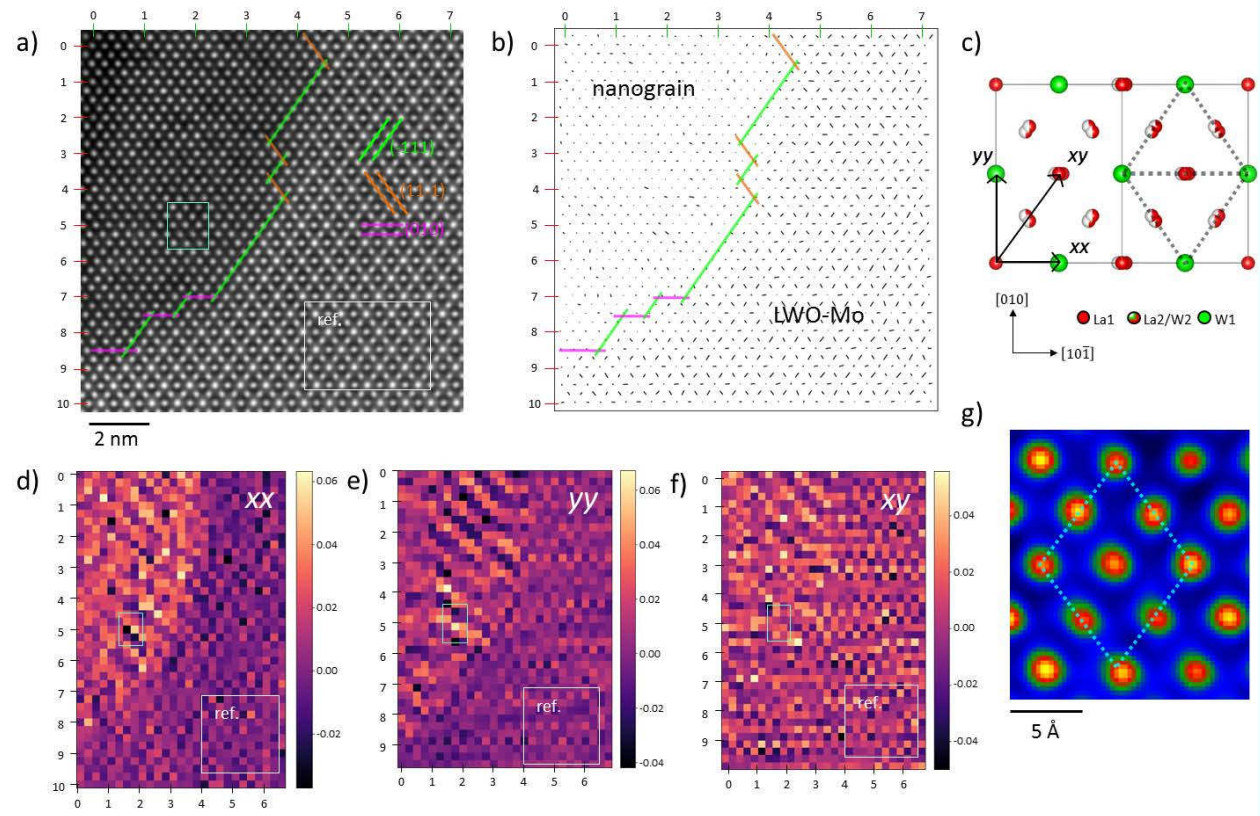

Fig. 5 Structural changes accompanying the grain boundary segregation. (a) HAADF image containing both LWO-Mo and the nanograin. Edge of the nanograin is indicated using relevant planes of LWO. The HAADF image is also scaled by the unit cell of LWO, as marked on the top and left. (b) Mapping the ellipticity of each atomic column in (a). (c) One unit cell of LWO oriented along [101] direction. (d-f) Strain maps estimated from (a), along *xx*, *yy* and *xy* directions as indicated in (c). The lower right part from LWO-Mo was used for reference, and the maps are scaled by the LWO unit cell. (g) Color-coded HAADF image cropped from the left rectangle region in (a).

Based on the average LWO model,[31] the La2/W2 sites are split and thus half occupied. As illustrated in Fig. 5c, when viewing along the [101] direction, elliptical atomic columns will be imaged, which are elongated along the connection between two nearest W sites.[28, 31] Fig. 5b maps the ellipticity of each atomic column in Fig. 5a, where the direction and magnitude of the elongation if any can be visualized through the angle and length of the bars.[32] Consistent with the model in Fig. 5c, regular elongations can be determined at the La2/W2 sites inside the LWO-Mo. In contrast, only a few elongations with much lower magnitudes and irregular directions are noticed inside the nanograin.

Taking the lower right part of the LWO-Mo as a reference, strains along *xx*, *yy* and *xy* direction as defined in Fig. 5c are estimated, in Fig. 5d-f. Along *xx*, up to 6% strain inside the nanograin can be measured. Along *yy*, generally positive strains are noticed, with certain fluctuations possibly due to the alternating (-111) and (11-1) planes along the SP-nanograin interface (see Fig. S5a in the ESI†). Fig. S5a shows that the nanograin/LWO-Mo is mainly separated from the SP through the (-111) plane, which is parallel to the *xy* direction. Meanwhile, in Fig. 5f, no specific strains along *xy* are observed inside the nanograin. Fig. 5g is the enlarged image of the left rectangle in Fig. 5a. Referring to the dotted rhombohedron, as sketched in Fig. 5c, the bottom middle atomic column is clearly shifting away from the lower vertex, ~35 pm along *xx*, ~ 176 pm along *yy* and ~ 20 pm along *xy*.

4. Discussion

The average model of LWO is derived from a fluorite structure with doubled lattice parameter owing to cation ordering. The La1 is mainly 8-fold coordinated in relatively symmetric cubes, the W1 forms WO_6 octahedra in alternating directions, and the La2 is coordinated with 6 or 7 Os in heavily distorted cubes. An additional W is incorporated in La2 sites as a donor self-dopant, which has implications to the conducting properties and the defect structure of the material.[33] Inside LWO, the oxygen vacancies were reported to have a slightly lower energy when occupying the O2 site and are bonded to the La1 and La2/W2 sites.[31]

Both the relaxation of the oxygen atoms around W1 sites to form a regular octahedron, and the relaxation of the 7-fold coordinated La2/W2 sites towards the nearest-neighbor WO_6 octahedron, account for the split of La2/W2 sites along the line connecting two W1 sites.[34] When the Zr^{4+} is replacing W^{6+} or Mo^{6+}, extra oxygen vacancies will be generated, and prone to stay at the O2 sites as it is energetically favorable.[31] As a result, the La2/W2 sites will be 6-fold instead of 7-fold coordinated.[35] For these 6-fold coordinated La2/W2 sites, it's then unnecessary to relax towards any neighboring WO_6

	$La(OH)_3$	WO_3	MoO_3	final membrane
Purity by Suppliers	99.95%	99.995%	99.97%	---
Zr [mg/kg]	<5	20 ± 2	<5	350 ± 20

Table 3 Results of the ICP-OES measurement of the three precursors ($La(OH)_3$, WO_3 and MoO_3) and the final membrane layer.

octahedron, which explains the much weaker splitting effect observed inside the nanograin. Moreover, with increased concentration of the oxygen vacancies, the onset temperature was reported to decrease, and a reduced stability of the membrane under the working condition would be expected.[36]

The Zr substitution of W and Mo accounts for the relatively lower contrast in Fig. 1b, 2a, 3a-b and 5a, as the lighter Zr appears darker than the heavier W and Mo in the Z-contrast image. Likewise, the strain inside the nanograin can be attributed to the larger ionic radius of Zr^{4+} (72 pm) than W^{6+} (60 pm) and Mo^{6+} (59 pm).[14] For the case in Fig. 3b and Fig. 5 (an interface between LWO-Mo and SP), the expansions are manifest in the direction perpendicular to the interface, and cause certain structural defects inside the neighboring SP. In contrast, parallel to the interface, the expansion is largely limited (see also Fig. S7 in the ESI†). Similar behaviors have been observed along other zone axis as well (see Fig. S8 in the ESI†). Thus, taking advantage of the relatively flexible structures of the SPs, strains built up inside the nanograin can be largely relaxed into the SP, leaving the surrounding LWO-Mo basically intact. However, local structural disorders would be inevitable when such kind of nanograins form between LWO-Mo grains (see Fig. S2 in the ESI†).

To clarify the origin of the Zr, inductively coupled plasma optical emission spectrometry (ICP-OES) was applied to the utilized precursors ($La(OH)_3$, WO_3 and MoO_3) and the final membrane. The results are listed in Table 3, which show ignorable contents of Zr in all the precursors but a significant amount in the final membrane. Meanwhile, for the powder and slurry preparation, ZrO_2 milling balls were intensively involved, and therefore can be considered as the main source of the detected Zr in the final membrane. Since the milling balls are essential for the membrane preparation, in order to effectively avoid any Zr contamination, proper alternatives for the widely used ZrO_2 should be considered. An ideal candidate would be both functionally and economically competent, while any component of it has an ignorable LWO-solubility. On the other side, some SPs showed the capability of accommodating the residual Zr (see Fig. S4 in the ESI†), as well as the structural flexibility of bearing strained nanograins. Thus, a careful introduction of certain SPs with a suitable amount can also be expected to improve the overall membrane performance.

5. Conclusions

In summary, a detailed study on the GBs inside LWO-Mo membranes has been performed. Resulting from the membrane processing, the residual Zr from the ZrO_2 milling balls segregates to the GBs, takes more than half of the W sites of the LWO-Mo, and leads to an expanded crystal structure. The specific form of the Zr segregation depends on the phase, orientation and contacting planes of the two neighboring grains, as well as the amount of the Zr. Due to the acceptor dopant $Zr_W^{\cdot\cdot}$, additional oxygen vacancies are generated, which significantly weaken the split at La2/W2 sites and lead to a decreased onset temperature of the membrane. All these GB features revealed by high-resolution TEM are closely related to the GB conductivity as well as the overall stability of the membrane. Moreover, considering the wide employment of ZrO_2 milling balls in the preparation of various types of ceramic membranes, our results can serve as a representative example, revealing how the processing procedures can influence the final membrane at the atomic scale and stimulating further studies towards promising optimized strategies for different membranes.

Conflicts of interest

There are no conflicts to declare.

Acknowledgements

We acknowledge support from the Bundesministerium für Bildung und Forschung (BMBF) under the Grant ProtOMem (03SF0537A and 03SF0537B). We thank Maximilian Kruth for preparation of the TEM lamellae by FIB.

References

1. T. Shimura, S. Fujimoto and H. Iwahara, *Solid State Ionics*, 2001, **143**, 117-123.
2. R. Haugsrud, *Solid State Ionics*, 2007, **178**, 555-560.
3. S. Escolastico, V. B. Vert and J. M. Serra, *Chem. Mater.*, 2009, **21**, 3079-3089.
4. S. Escolastico, C. Solis and J. M. Serra, *Int. J. Hydrogen Energy*, 2011, **36**, 11946-11954.
5. S. Escolastico, C. Solis and J. M. Serra, *Solid State Ionics*, 2012, **216**, 31-35.
6. S. Escolastico, C. Solis, T. Scherb, G. Schumacher and J. M. Serra, *J. Membr. Sci.*, 2013, **444**, 276-284.
7. S. Escolastico, J. Seeger, S. Roitsch, M. Ivanova, W. A. Meulenberg and J. M. Serra, *Chemsuschem*, 2013, **6**, 1523-1532.
8. M. E. Ivanova, W. Deibert, D. Marcano, S. Escolastico, G. Mauer, W. A. Meulenberg, M. Bram, J. M. Serra, R. Vassen and O. Guillon, *Sep. Purif. Technol.*, 2019, **219**, 100-112.
9. S. Escolastico, C. Solis, C. Kjolseth and J. M. Serra, *Energy Environ. Sci.*, 2014, **7**, 3736-3746.
10. M. E. Ivanova, S. Escolastico, M. Balaguer, J. Palisaitis, Y. J. Sohn, W. A. Meulenberg, O. Guillon, J. Mayer and J. M. Serra, *Sci. Rep.*, 2016, **6**, 34773.
11. H. Q. Xie, L. B. Zhuang, Y. Y. Wei, J. Xue and H. H. Wang, *Ceram. Int.*, 2017, **43**, 14608-14615.
12. L. Chen, L. B. Zhuang, J. Xue, Y. Y. Wei and H. H. Wang, *J. Mater. Chem. A*, 2017, **5**, 20482-20490.

13. J. Seeger, M. E. Ivanova, W. A. Meulenberg, D. Sebold, D. Stover, T. Scherb, G. Schumacher, S. Escolastico, C. Solis and J. M. Serra, *Inorg. Chem.*, 2013, **52**, 10375-10386.
14. R. D. Shannon, *Acta Crystallogr., Sect. A: Found. Crystallogr.*, 1976, **32**, 751-767.
15. M. Amsif, A. Magraso, D. Marrero-Lopez, J. C. Ruiz-Morales, J. Canales-Vazquez and P. Nunez, *Chem. Mater.*, 2012, **24**, 3868-3877.
16. W. Deibert, M. E. Ivanova, W. A. Meulenberg, R. Vassen and O. Guillon, *J. Membr. Sci.*, 2015, **492**, 439-451.
17. W. Deibert, F. Schulze-Kuppers, E. Forster, M. E. Ivanova, M. Muller and W. A. Meulenberg, *J. Eur. Ceram. Soc.*, 2017, **37**, 671-677.
18. M. L. Fontaine, C. Denonville, Z. A. Li, W. Xing, J. M. Polfus, J. Kvello, J. S. Graff, P. I. Dahl, P. P. Henriksen and R. Bredesen, *J. Eur. Ceram. Soc.*, 2018, **38**, 1695-1701.
19. Y. Lin, S. M. Fang, D. Su, K. S. Brinkman and F. L. Chen, *Nat. Commun.*, 2015, **6**, 6824.
20. H. S. Kim, H. B. Bae, W. Jung and S. Y. Chung, *Nano Lett.*, 2018, **18**, 1110-1117.
21. J. An, J. S. Park, A. L. Koh, H. B. Lee, H. J. Jung, J. Schoonman, R. Sinclair, T. M. Gur and F. B. Prinz, *Sci. Rep.*, 2013, **3**, 2680.
22. Y. Y. Lei, Y. Ito, N. D. Browning and T. J. Mazanec, *J. Am. Ceram. Soc.*, 2002, **85**, 2359-2363.
23. D. Meertens, M. Kruth and K. Tillmann, *Journal of large-scale research facilities*, 2016, **2**, A60.
24. A. Kovács, R. Schierholz and K. Tillmann, *Journal of large-scale research facilities*, 2016, **2**, A43.
25. D. Park, A. Herpers, T. Menke, M. Heidelmann, L. Houben, R. Dittmann and J. Mayer, *Microsc. Microanal.*, 2014, **20**, 740-747.
26. H. C. Du, *Ultramicroscopy*, 2015, **151**, 62-67.
27. K. Momma and F. Izumi, *J. Appl. Crystallogr.*, 2011, **44**, 1272-1276.
28. K. Ran, W. Deibert, M. E. Ivanova, W. A. Meulenberg and J. Mayer, *Sci. Rep.*, 2019, **9**, 3274.
29. K. Ran, W. Deibert, H. C. Du, D. Park, M. E. Ivanova, W. A. Meulenberg and J. Mayer, *Acta Mater.*, 2019, **180**, 35-41.
30. J. Yuan, T. Hirayama, Y. Ikuhara and T. Sakuma, *Micron*, 1999, **30**, 141-145.
31. A. Fantin, T. Scherb, J. Seeger, G. Schumacher, U. Gerhards, M. E. Ivanova, W. A. Meulenberg, R. Dittmeyer and J. Banhart, *J. Appl. Crystallogr.*, 2016, **49**, 1544-1560.
32. M. Nord, P. E. Vullum, I. MacLaren, T. Tybell and R. Holmestad, *Adv. Struct. Chem. Imaging*, 2017, **3**, 9.
33. L. E. Kalland, A. Magraso, A. Mancini, C. Tealdi and L. Malavasi, *Chem. Mater.*, 2013, **25**, 2378-2384.
34. T. Scherb, S. A. J. Kimber, C. Stephan, P. F. Henry, G. Schumacher, S. Escolastico, J. M. Serra, J. Seeger, J. Just, A. H. Hill and J. Banhart, *J. Appl. Crystallogr.*, 2016, **49**, 997-1008.
35. A. Fantin, T. Scherb, J. Seeger, G. Schumacher, U. Gerhards, M. E. Ivanova, W. A. Meulenberg, R. Dittmeyer and J. Banhart, *J. Appl. Crystallogr.*, 2019, **52**, 1043-1053.
36. A. Fantin, T. Scherb, J. Seeger, G. Schumacher, U. Gerhards, M. E. Ivanova, W. A. Meulenberg, R. Dittmeyer and J. Banhart, *Solid State Ionics*, 2017, **306**, 104-111.

Table of Contents

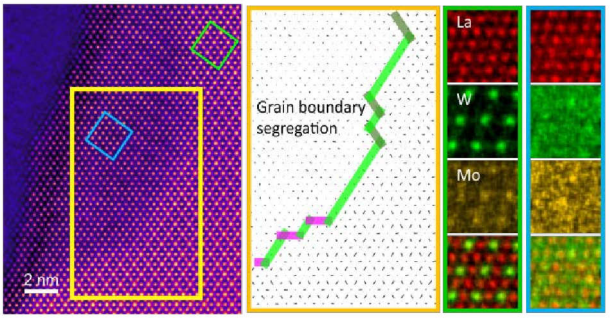

Membrane processing induced grain boundary segregation revealed with atomic resolution